Engineering Structures 197 (2019) 108874

Contents lists available at ScienceDirect

Engineering Structures

journal homepage: www.elsevier.com/locate/engstruct

Shape optimization of U-shaped steel dampers subjected to cyclic loading using an efficient hybrid approach

Mohsen Khatibinia[a,*], Mehdi Jalaipour[a], Sadjad Gharehbaghi[b]

[a] Department of Civil Engineering, University of Birjand, Birjand, Iran
[b] Department of Civil Engineering, Behbahan Khatam Alanbia University of Technology, Behbahan, Iran

ARTICLE INFO

Keywords:
U-shaped steel damper
Cyclic Loading
Energy dissipation
Shape optimization
Support vector machine
Particle swarm optimization algorithm

ABSTRACT

U-shaped steel damper (USSD), as an energy dissipation device, has been recommended in the literature for using in the isolation systems. This type of damper is capable of appropriately dissipating the input energy which a structure imparts from an earthquake. The capability is provided through a large range of plastic deformations occurred in the USSD. This paper aimed at presenting a methodology structured in the framework of a shape optimization problem to enhance the seismic energy dissipation and deformation capability of the USSD under cyclic loading. To achieve this goal, the straight part, thickness and height of the USSD were considered as the design variables of the optimization problem and optimized through maximizing the ratio of energy dissipation through plastic deformation to the maximum equivalent plastic strain. In order to find the optimum shape of the USSD under cyclic loading, a hybrid approach consisted of two phases was applied. In the first phase, as an alternative for the time-consuming finite element analysis, a support vector machine (SVM) approach was trained, tested and used to predict the inelastic responses of the USSD. In the second phase, a modified particle swarm optimization (PSO) algorithm was adopted to find the optimum shape of the USSD subjected to two critical directions of cyclic loading. After finding the optimum shape of the USSD, the energy dissipation and deformation capability of the optimum shaped-USSD were assessed. Results demonstrate that the proposed shape optimization methodology renders an optimum-shaped USSD with significantly improved energy dissipation and deformation capability compared with those of available in the literature.

1. Introduction

Conventional seismic design approaches of structures rely on the strength, stiffness, and inelastic deformation capacity so that the structures can withstand a given level of design earthquake. However, mitigating the structural damage with economic considerations is the main goal of the modern seismic design methodologies. One of their solutions is to mitigate the seismic input energy before dissipating it by means of the structural elements [1,2]. In this regard, some devices including Added Damping and Stiffness (ADAS) and Triangular Added Damping and Stiffness (TADAS) elements [3–5], Shear panels [6–11], Shear panels with openings [12–16], Buckling-Restrained Braces (BRBs) [17–20] and U-shaped steel dampers (USSDs) [21–23] have been produced and their efficiency have been demonstrated based on theoretical studies and experiments.

As one of the first metallic dampers, the USSD was proposed in order to dissipate the seismic input energy through creating its post-elastic deformations. The first idea for using the USSD in the design of structures was proposed by Kelly et al. [24] in 1972 and investigated in the framework of a conceptual and experimental work. After two decades, Aguirre and Sánchez [25] implemented a set of experiments in order to investigate and confirm the energy absorbing capability and determine the properties of energy dissipation of the USSD. Dolce et al. [26] proposed a type of the USSD which was arranged in a radial pattern. The proposed passive device using its elasto-plastic biaxial behavior can protect and control structures. They implemented the experimental tests and the numerical simulation in order to prove the potential application of this device for the seismic control of engineering structures. Furthermore, this device as a seismic isolator in bridge piers was proposed and used in Italy [27].

The satisfactory performance of the USSD enabled it to use in conjunction with rubber bearings to improve the overall damping of the system (see Fig. 1). Moreover, this device has been separately set up at various locations of an isolation system. Hence, after 1995 Kobe earthquake, the application of this device widely increased to protect hospitals, plants and residential buildings in Japan [22]. In addition,

* Corresponding author.
E-mail address: m.khatibinia@birjand.ac.ir (M. Khatibinia).

https://doi.org/10.1016/j.engstruct.2019.02.005
Received 19 August 2018; Received in revised form 31 January 2019; Accepted 2 February 2019
Available online 30 July 2019
0141-0296/

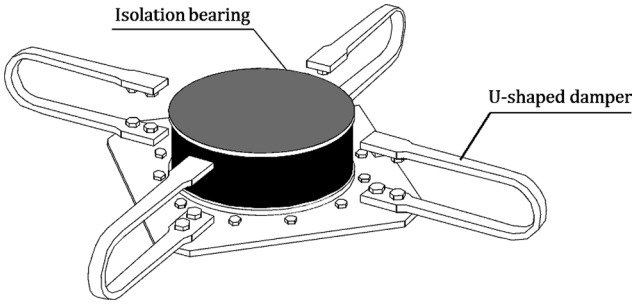

Fig. 1. U-shaped steel dampers (USSDs) installed around an isolation bearing.

more studies for the assessment of this device have been carried out by researchers which some of them are presented herein. Deng et al. [28] developed a novel crawler steel damper which was used in the isolation layer of bridges. The new device consists of two USSDs and two connection plates. The plates located in the top and bottom of USSDs are bolted to them. Bagheri et al. [29] proposed and assessed the use of USSD with inverted V-braces in steel buildings. The results of their seismic evaluation revealed that the maximum base shear and roof displacement are significantly reduced by adding this damper in inverted V-braces. Jiao et al. [22] implemented the experimental study on full-scale U-dampers in order to investigate and demonstrate their hysteretic behavior and low-cycle fatigue characteristics subjected to various loading directions, loading speeds and temperatures. Ene et al. [23] investigated the fatigue behavior of the USSD subjected to bidirectional loading. For this purpose, full-scale specimens were selected and experimented for two sets of loading tests consisting of quasi-static tests with simple histories and dynamic tests with realistic loading histories.

In the past decades, the subject of structural optimization as an interesting area of research has attracted considerable attention among researchers. The structural optimization could be used to enhance the structural characteristics such as reducing stress concentration, structural weight, and maximum displacements [30]. As a general classification, the structural optimization includes sizing, shape and topology optimization. The main purpose of the shape optimization is to find the optimum geometry of a design domain with known loading and boundary conditions [31,32]. Reviews of early studies on the shape optimization could be found in Olhoff and Rozvany [33], and Munk et al. [34]. Recently, Deng et al. [35] proposed an optimum shape for the USSD to improve its hysteretic behavior under cyclic loading. In their study, the length and width of the USSD straight part were only considered as the optimization variables while the effect of other parameters including the thickness and height of the USSD were not investigated on the optimum shape of the USSD. Moreover, since the least squares method was used to solve the optimization problem, it is expected that their presented optimum shape of the USSD is not necessarily a global optimum solution.

Previously, gradient based algorithms have been widely used to solve many engineering optimization problems. Concerning the complex problems, finding the global optima of their governing function with the large number of local optima could not be easily obtained by a gradient based algorithm. In fact, as they solve the optimization problems by computing derivations, they are not reliable and tend to get trapped in local optima [36]. In the last decades, many new gradient-free based algorithms have been developed and used in solving the large number of engineering optimization problems. Contrary to gradient based algorithms, these optimization algorithms have stochastic basis providing a condition for them to escape from local optima. Although these optimization algorithms are computationally expensive leading to slower convergence rate, they have been widely used to find near global optimum solution. Among them, a nature-inspired stochastic optimization algorithm, namely particle swarm optimization (PSO), has successfully been used by researchers. Because of its efficient exploration mechanism, few needed parameters and simplicity, PSO has been extensively used to find the near optimum solution in the last years. These features leads to lower computational cost compared with other heuristic algorithms.

The main contribution of this paper is to improve the energy dissipation and deformation capability of the USSD subjected to cyclic loading applied in two critical directions of 90° and 45°. This aim was structured in the framework of a shape optimization problem. In this study, a single objective function was adopted for the shape optimization problem such that it results in an improvement in the energy dissipation and deformation capability of the USSD. The straight part, thickness, width and height of the USSD were considered as the optimization variables. An efficient hybrid approach was used to find the optimum shape of the USSD. It employs a modified PSO algorithm based on the passive congregation called (PSOPC) [37] and a weighted least squares support vector machine (WLS-SVM) [38]. The PSOPC algorithm, as an efficient algorithm, was adopted to solve the defined shape optimization problem. The inelastic finite element analysis of the USSD needs an expensive computational burden particularly when it is subjected to cyclic loading. This computational burden is accentuated when an iterative procedure is used to find the optimum solution. Motivated by this crucial need, accurately predicting the inelastic responses of the USSD is of great importance resulting in substantially reducing the computational burden. Since, the feasibility of the optimum design greatly depends on the accuracy of the predicted responses, the WLS-SVM approach, as an efficient computational tool, was used in this study. The formulations, assumptions, procedure and findings are described in the next sections.

2. Shape optimization problem of USSD

One of the important steps of structural design problems is the process of determining the structural shape dimensions that could be structured in the framework of an optimization process. This process is called as structural shape optimization in which the exterior and interior boundaries of a structure is determined [33]. In this study, this process is used to determine the optimum shape of the USSD subjected to cyclic loading. An experimental study was carried out by Deng et al. [35] in order to find the effect of the straight parts of this damper on its behavior. Based on their work, it can be concluded that the engineering design of these parts could prevent the plastic strain concentration and unrecoverable deformations resulting in an efficient performance. In effect, the main influential dimensions of the USSD are the width and the length of the straight part, and its thickness and height. Hence, in this study, these dimensions were considered as the design variables of a single-objective shape optimization problem (see Fig. 2). In order to improve the energy dissipation and deformation capability of the USSD subjected to cyclic loading, maximizing the ratio of *energy dissipation through plastic deformation* (*ALLPD*) to *maximum equivalent plastic strain* ($PEEQ_{max}$) was adopted as the objective function of the shape optimization problem which could be defined as follows:

$$\begin{aligned} &\text{Finde: } \boldsymbol{X} = \{b_2, L, H, t\} \\ &\text{Maximize: } F(\boldsymbol{X}) = \frac{ALLPD}{PEEQ_{\max}} \end{aligned} \tag{1}$$

The parameters b_2, L, H and t respectively are the width of second end of the straight part (at the first of curved part), the length of the straight part, and thickness and height of the USSD and are shown in Fig. 2. In this study, two directions of 90° and 45° were used to apply the cyclic loading on the USSD.

3. Particle swarm optimization algorithm

In this study, the optimum shape of the USSD was found using a modified particle swarm optimization (PSO) algorithm. In the recent

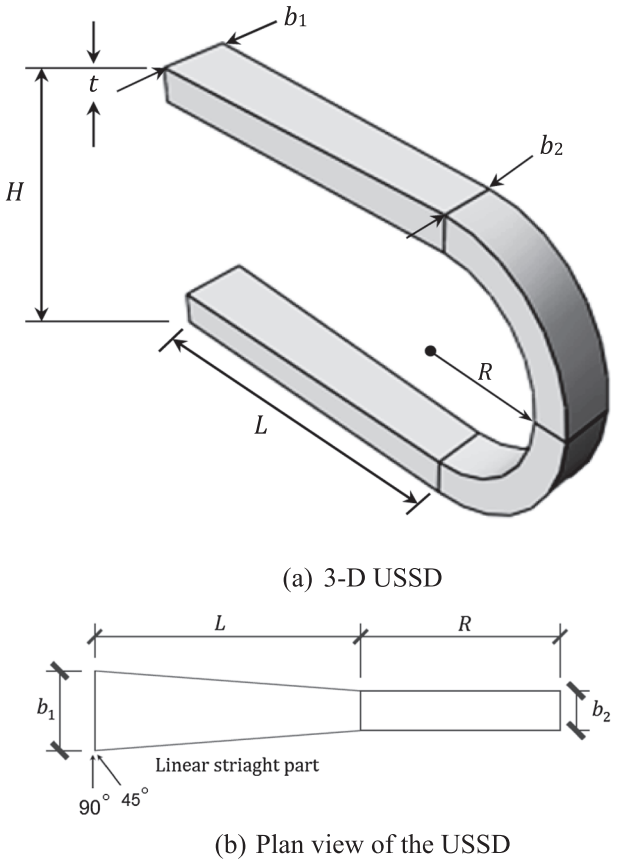

Fig. 2. The parameters (dimensions) of the USSD shape optimization.

years, PSO as a heuristic global optimization method have been successfully used in the optimization problems of engineering structures [39–41]. This method introduced by Kennedy and Eberhart [42] in the mid-1990s has been simulated based on the movement of bird swarm or fish school. In the PSO, each bird is considered as a possible solution in the search space of optimization problem and is recognized as a particle. At first, a group of particles as swarm is randomly generated and located in the search space. Then, the search procedure begins to reach the most suitable responses using an iterative procedure. In each iteration, the particles move towards the most proper locations. The movement direction of each one depends on three parameters including its velocity, its best known position (p_{best}) and the best known position of the bird swarm (g_{best}) that the birds have obtained since the first iteration [42]. This iterative procedure continues until the velocity of the birds' movement is equal to zero or the number of iterations reaches a maximum reasonable number of iterations.

In tth iteration of the PSO, the ith particle has a position vector, $\boldsymbol{X}_i^t$, and a velocity vector, $\boldsymbol{V}_i^t$, that are presented as follow:

$$\begin{aligned} \boldsymbol{X}_i^t &= \{ x_{i,1}^t,\ x_{i,2}^t,\ \ldots,\ x_{i,N}^t \} \\ \boldsymbol{V}_i^t &= \{ v_{i,1}^t,\ v_{i,2}^t,\ \ldots,\ v_{i,N}^t \} \end{aligned} \tag{2}$$

where N is the dimension of the problem space. In $(t + 1)$th iteration of the PSO, the ith particle can fly in the solution space of optimization problem and its position is updated as [42]:

$$\boldsymbol{V}_i^{t+1} = \omega^t \boldsymbol{V}_i^t + c_1 r_1 (\boldsymbol{p}_{\boldsymbol{best},i}^t - \boldsymbol{X}_i^t) + c_2 r_2 (\boldsymbol{g}_{\boldsymbol{best}}^t - \boldsymbol{X}_i^t) \tag{3}$$

$$\boldsymbol{X}_i^{t+1} = \boldsymbol{X}_i^t + \boldsymbol{V}_i^{t+1} \tag{4}$$

where r_1 and r_2 are the uniform random number in interval [0, 1]; c_1 and c_2 are the cognitive and social scaling factor, respectively; and ω^t is considered as the inertia weight factor which has an important role in the PSO and prevents quick convergence of the PSO as follows [43]:

$$\omega = \omega_{\max} - \frac{\omega_{\max} - \omega_{\min}}{t_{\max}} t \tag{5}$$

where $\omega_{\max}$ and $\omega_{\min}$ are the maximum and minimum values of ω, respectively; and $t_{\max}$ is the maximum number of optimization iteration.

In order to overcome the shortcoming of trapping local optimum in the PSO, He et al. [37] presented a modified PSO based on the passive congregation, called (PSOPC). It was demonstrated that this modification efficiently improve the convergence rate and accuracy of PSO algorithm. In the proposed PSOPC, the velocity of the ith particle is modified as:

$$\boldsymbol{V}_i^{t+1} = \omega^t \boldsymbol{V}_i^t + c_1 r_1 (\boldsymbol{p}_{\boldsymbol{best},i}^t - \boldsymbol{X}_i^t) + c_2 r_2 (\boldsymbol{g}_{\boldsymbol{best}}^t - \boldsymbol{X}_i^t) + c_3 r_3 (\boldsymbol{R}^t - \boldsymbol{X}_i^t) \tag{6}$$

where $\boldsymbol{R}$ is the position vector of a particle which is randomly selected from the swarm in the tth iteration, c_3 the passive congregation factor, and r_3 is a uniform random number in interval (0, 1).

4. Finite element model and analysis of USSD

In this paper, finite element (FE) method was adopted to model and analysis of the USSD. The assumptions and verification of FE method for modeling the USSD are explained in this section.

4.1. FE modeling of USSD

The FE modeling and analysis of the USSD were accomplished by a Python script in the FE package ABAQUS [44]. The brick element (named as C3D8R), which is an 8-node element with reduced integration and hourglass control, was used for modeling the behavior of the USSD. The combined isotropic/kinematic hardening as the constitutive law was employed to explain the cyclic behavior of the USSD material. In the numerical material law, the nonlinear kinematic hardening component is obtained by superimposing two or more nonlinear kinematic hardening models as [45]:

$$\alpha = \sum_{k=1}^{n} \frac{C_k}{\gamma_k} \left(1 - e^{-\gamma_k \bar{\varepsilon}^{pl}}\right) \tag{7}$$

where n is the number of back-stresses; C and γ are the material parameters that are calibrated from cyclic test data. C is the initial kinematic hardening module, γ determines the rate at which the kinematic hardening module decreases with increasing plastic deformation. $\bar{\varepsilon}^{pl}$ is considered as the equivalent plastic strain, called *PEEQ*.

The yield surface size of material is evaluated by the isotropic hardening component, which is expressed by a function of *PEEQ* as following [46]:

$$\sigma^0 = \sigma_0 + Q_\infty \left(1 - e^{-b\bar{\varepsilon}^{pl}}\right) \tag{8}$$

where σ^0 is the initial yield stress at zero plastic strain; Q_∞ and b are the material parameters. Q_∞ is the maximum change in the size of the yield surface.

The total energy dissipation through plastic deformations, denoted by *ALLPD*, is obtained by performing a post-processing on the ABAQUS outputs and is defined as follows [44]:

$$ALLPD = \int_V \int_0^{\bar{t}} \boldsymbol{\sigma} : \dot{\boldsymbol{\varepsilon}}^{pl} d\bar{t}\, dV \tag{9}$$

where $\boldsymbol{\sigma}$ and $\dot{\boldsymbol{\varepsilon}}^{pl}$ are the stress tensor and the incremental plastic strains, respectively; V is the total volume of the USSD; and $\bar{t}$ is the duration of the loading applied.

Since the connection parts of the USSD including bolts, steel plates and heads are designed for staying in the elastic state during loading, herein, only the second part (straight part) and the curved part of the USSD (see Fig. 2) were considered in the FE modeling.

Table 1
The material properties of the UD40 [22].

Yield strength (N/mm^2)	Tensile strength (N/mm^2)	Yield ratio (%)	Elongation (%)
378	544	69	37

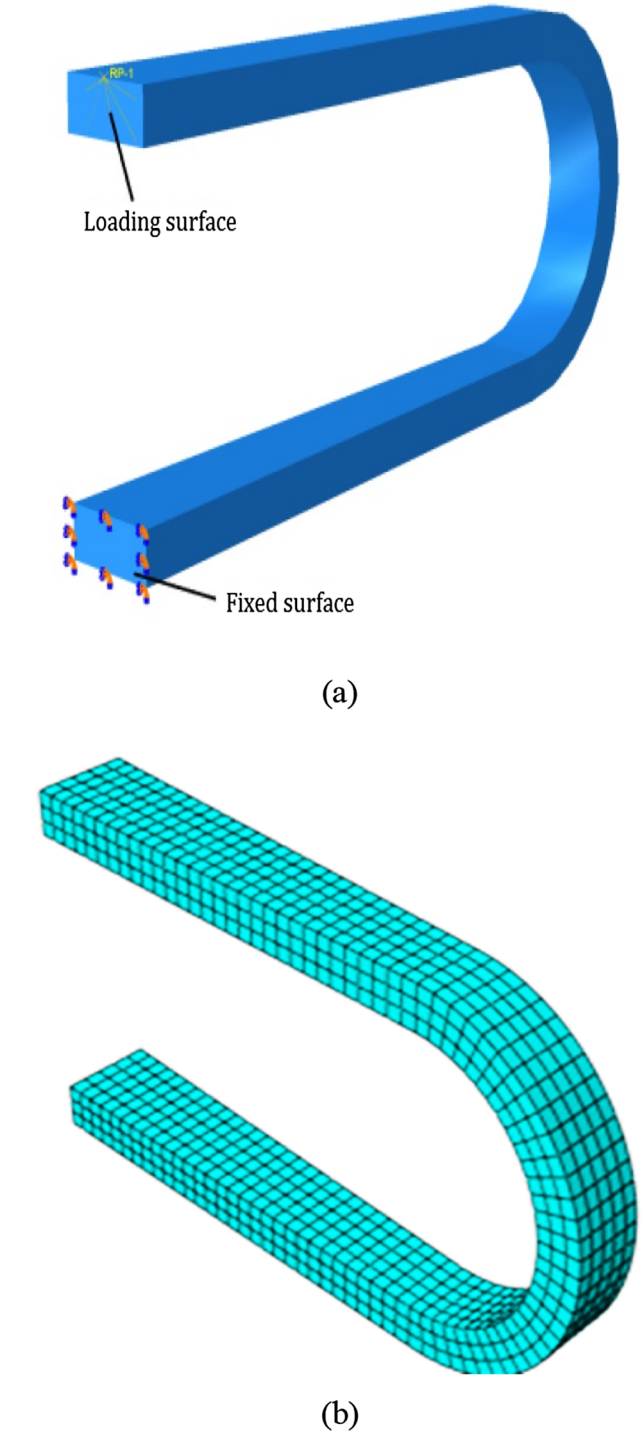

Fig. 3. (a) The geometry and (b) meshing configuration of the UD40 FE model.

4.2. Verification of the FE modeling

The accuracy of FE model used in this study was validated by a comprehensive experimental test conducted on a USSD type named as UD40. The experimental data and dimensions of the USSD model is available in the work by Jiao et al. [22]. The dimensions of the UD40 including the length of the straight part (L), the width of two ends of straight part (b_1) and (b_2), the thickness (t) and the height (H) are 185, 60 and 45, 28 and 231 mm, respectively. In the experimental study [22], the damper was statically loaded with a monotonic deformation amplitude of 500 mm separately in both 0° and 90° directions. According to the coupon tests [22], the material properties used for the FE model are listed in Table 1.

In the elastic-plastic analysis of the FE model, the balance between computational accuracy and efficiency are sensitive to the size of meshes. In order to validate the FE model with respect to the experimental results, the meshing element size was finally selected to be 5 mm. The geometry and meshing configuration of the FE model of UD40 are shown in Fig. 3.

In order to validate the FE model of the UD40, the model was subjected to monotonic loading in two directions of 0 and 90°, and their pushover curves were derived and compared with those for the experimental tests reported in the work [22]. The pushover curves are shown in Fig. 4(a) and (b). As shown, the curves related to the FE model is in a good agreement with those for the experimental tests [22].

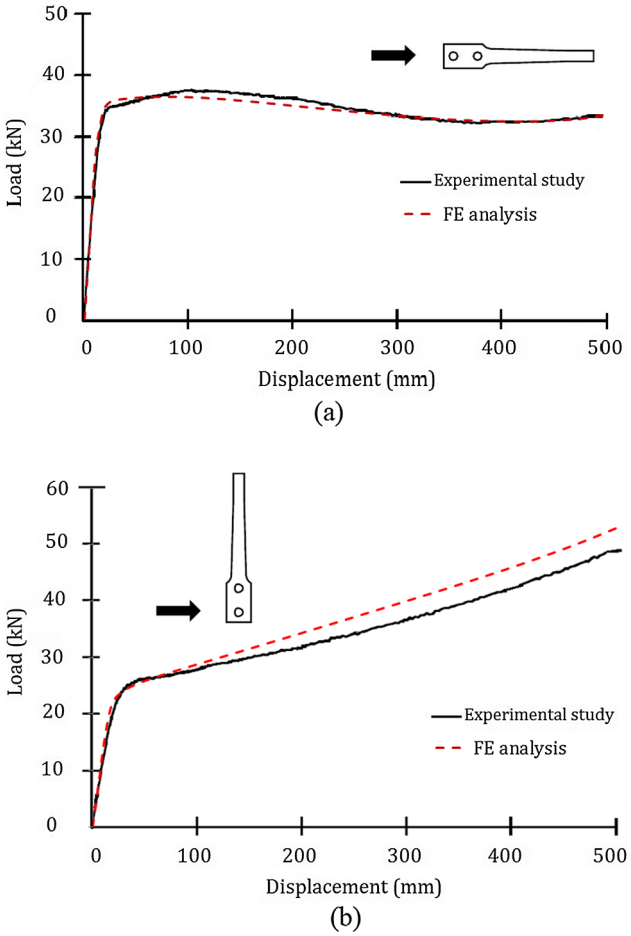

Fig. 4. Comparison between the pushover curves for FE analysis (this paper) and the experimental study [22] for (a) 90° and (b) 45°.

5. WLS-SVM approach

Support vector machines (SVMs) are a proper set of supervised learning models to solve the complex and time-consuming problems in which the process and map input to higher-dimensional feature spaces. SVMs-based approaches could be the best choice to solve the problems

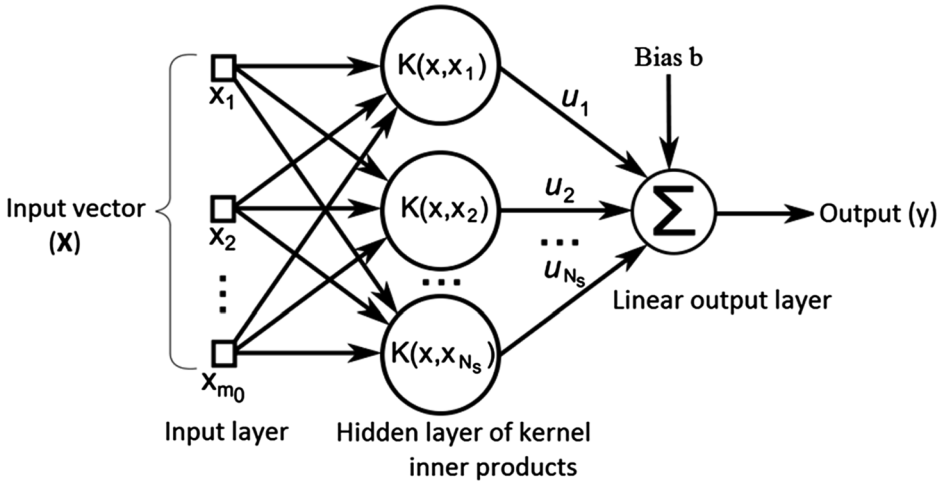

Fig. 5. The structure of the WLS-SVM model.

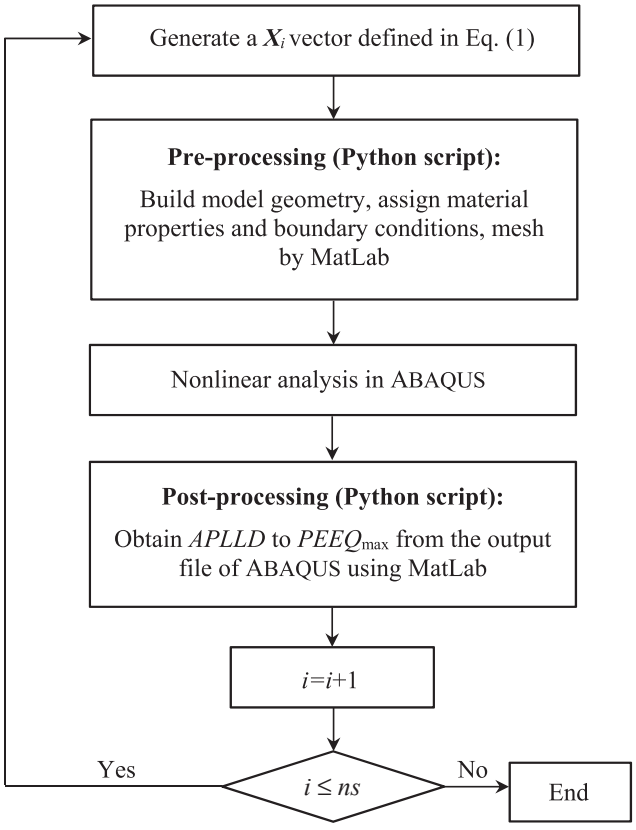

Fig. 6. Flowchart of dataset generation.

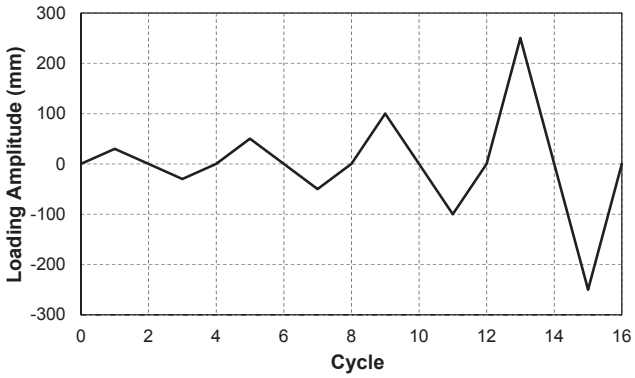

Fig. 7. Loading protocol for the FE analysis of the USSD [22].

Table 2
Lower and upper bounds for the dimensions of the USSD.

Parameter	Lower bound (mm)	Upper bound (mm)
H	200	400
L	200	400
b_2	30	70
t	15	30

Table 3
Performance metrics for the WLS-SVM model in the testing mode.

Loading direction	*MAPE*	*RRMSE*	R^2
45°	2.910	0.0435	0.9981
90°	3.458	0.0516	0.9973

which require much computational effort in prediction and evaluation of the actual responses of a complex system. These approaches work well even by training a restricted set of data where data are not available or determining them needs a time-consuming process. In recent years, the WLS-SVM approach has shown an excellent performance in solving many structural problems [47–51]. This approach is briefly described in this section.

The WLS-SVM approach introduced by Suykens et al. [38] has been proposed for modeling the highly non-linear systems based on small samples. The WLS-SVM model has been defined as an optimization problem in a primal weight space as follows [38]:

$$\text{Minimize } J(\omega,\ \xi) = \frac{1}{2}\omega^T\omega + \frac{1}{2}\gamma\sum_{i=1}^{n} w_i\xi_i^2$$
$$\text{Subject to } y_i = \omega^T\phi(\boldsymbol{X}_i) + b + \xi_i, \quad i = 1,\ 2,\ \ldots, n \tag{10}$$

which $\{\boldsymbol{X}_i, y_i\}_{i=1}^n$ is a training data set, $\boldsymbol{X}_i \in R^n$ is input data, and $y_i \in R$ is output data. $\phi(.)$: $R^n \rightarrow R^d$ is considered as a function for mapping the input space into a higher dimensional space. $\omega \in R^d$ represents a weight vector in the primal weight space. $\xi_i \in R$ and $b \in R$ are the error variable and the bias term, respectively.

The Lagrange multiplier technique is adopted in order to solve the dual problem (i.e. Eq. (10)) as:

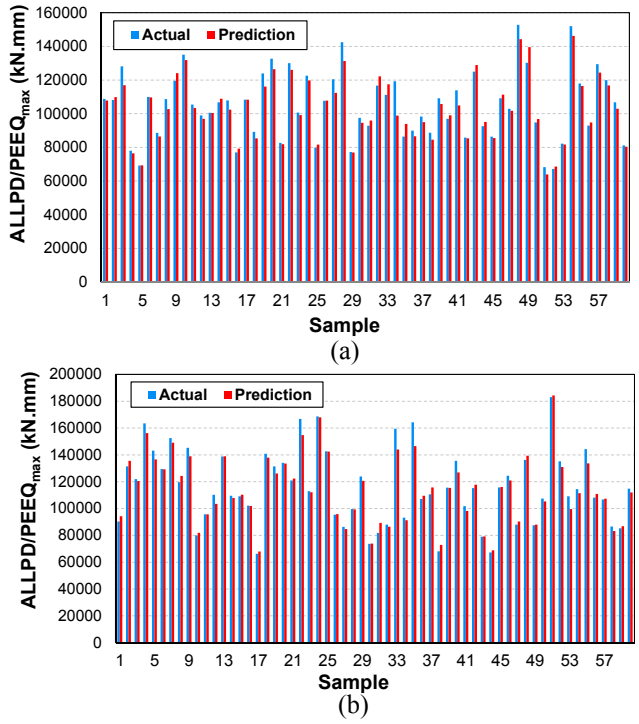

Fig. 8. Comparison of actual and predicted *ALLPD/PEEQ*$_{max}$ for (a) 90° and (b) 45° loading direction.

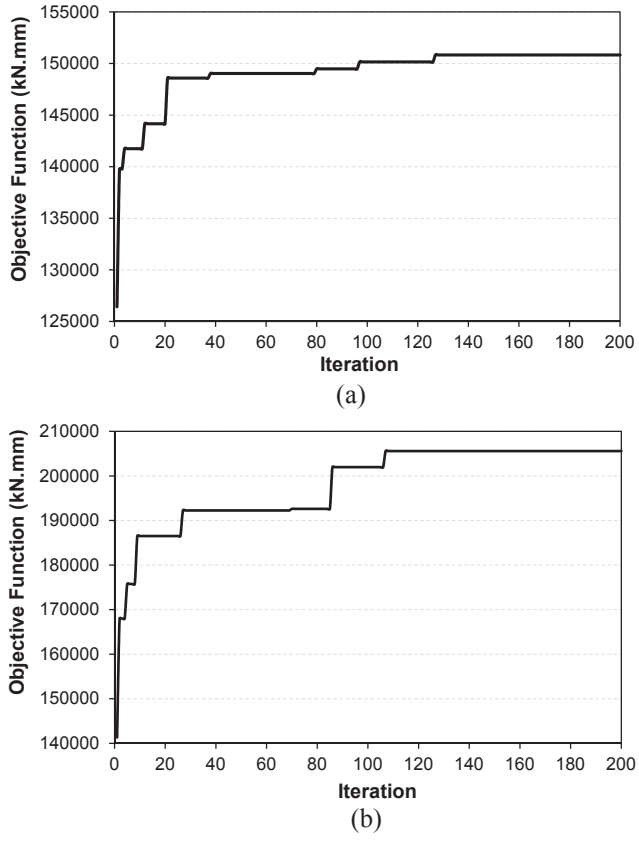

Fig. 9. Convergence of optimization process for (a) 90° and (b) 45° loading direction.

Table 4
The assumed different values of the input parameters of the PSOPC algorithm.

Case	c_1	c_2	c_3	ω_{max}	ω_{min}
1	2	2	0.6	0.4	0.1
2	2	2	0.6	0.9	0.4
3	2	2	0.5	0.4	0.1
4	2	2	0.5	0.9	0.4
5	1.5	2	0.6	0.4	0.1
6	1.5	2	0.6	0.9	0.4
7	1.5	2	0.5	0.4	0.1
8	1.5	2	0.5	0.9	0.4
9	1	2	0.6	0.4	0.1
10	1	2	0.6	0.9	0.4
11	1	2	0.5	0.4	0.1
12	1	2	0.5	0.9	0.4
13	0.5	1.5	0.6	0.4	0.1
14	0.5	1.5	0.6	0.9	0.4
15	0.5	1.5	0.5	0.4	0.1
16	0.5	1.5	0.5	0.9	0.4

$$L(\omega,\ b,\ \xi,\ \alpha) = J(\omega,\ \xi) - \sum_{i=1}^{n} \alpha_i(\omega^T \phi(\boldsymbol{X}_i) + b + \xi_i - y_i) \tag{11}$$

According to the Karush-Khun-Tucker conditions, after optimizing Eq. (10) and eliminating $\boldsymbol{\omega}$ and ξ, the solution of the problem is obtained using the following set of linear equations:

$$\begin{bmatrix} \boldsymbol{\Omega} + \boldsymbol{V}_\gamma & \mathbf{1}_n^T \\ \mathbf{1}_n & \mathbf{0} \end{bmatrix} \begin{bmatrix} \boldsymbol{\alpha} \\ b \end{bmatrix} = \begin{bmatrix} \boldsymbol{y} \\ 0 \end{bmatrix} \tag{12}$$

where $\boldsymbol{V}_\gamma = diag\{1/\gamma\,\bar{v}_1,\ \ldots,1/\gamma\,\bar{v}_n\}$; $\boldsymbol{\Omega}$ is $n \times n$ Hessian vector and is defined as $\Omega_{i,j} = \langle \phi(\boldsymbol{X}_i), \phi(\boldsymbol{X}_j)\rangle_H = K(\boldsymbol{X}_i, \boldsymbol{X}_j)$. $K(.,.)$ is a kernel function. In this study, the radial basis function is selected as the kernel function of the WLS-SVM model and is expressed as follows:

$$K(\boldsymbol{X}_i,\ \boldsymbol{X}_j) = \exp\left(-\frac{\|\boldsymbol{X}_i - \boldsymbol{X}_j\|^2}{2\,\sigma^2}\right) \tag{13}$$

Therefore, the WLS-SVM model for the prediction of functions is obtained as follows:

$$y(\boldsymbol{X}) = \sum_{i=1}^{n} \alpha_i K(\boldsymbol{X}_i, \boldsymbol{X}) + b \tag{14}$$

where $\boldsymbol{\alpha}$ and b are the solutions to the problem expressed by Eq. (12). The parameters represent the high dimensional feature spaces that are non-linearly mapped from the input space $\boldsymbol{X}$. Furthermore, the predicted value of y is obtained using the model presented in Eq. (14). The overall structure of the WLS-SVM model is depicted in Fig. 5.

6. Prediction of USSD responses using WLS-SVM

To solve the iterative procedure of shape optimization of the USSD, a large number of the FE analyses of the USSD subjected to cycle loading are required to be run in the ABAQUS software. This procedure is time-consuming and it needs expensive computational burden. To eliminate this shortcoming, the WLS-SVM approach was used to predict the inelastic responses of the USSD required during the optimization procedure. In this regard, WLS-SVM was trained and tested using a randomly generated database including a required number of USSDs which are different to each other in terms of the design variables mentioned. The design variables of the USSD and the *ALLPD* to *PEEQ*$_{max}$ ratio (as the objective function of the defined shape optimization problem) were considered as the input and output of the WLS-SVM model, respectively. The inputs and output vectors of the WLS-SVM model could be represented as follows:

$$\boldsymbol{I}_{WLS-SVM} = \{\boldsymbol{X}_1, \boldsymbol{X}_2,\ \ldots,\boldsymbol{X}_{ns}\} \tag{15}$$

$$\boldsymbol{O}_{WLS-SVM} = \{F_1, F_2,\ \ldots,F_{ns}\} \tag{16}$$

Table 5
The optimum results obtained by using PSO algorithm for different cases.

Case	45°					90°				
	H (mm)	L(mm)	b_2 (mm)	t (mm)	$F(\boldsymbol{X})$ (kN.mm)	H (mm)	L(mm)	b_2 (mm)	t (mm)	$F(\boldsymbol{X})$ (kN.mm)
1	243.47	370.87	48.68	29.02	205415.250	258.52	278.87	45.98	28.78	148989.589
2	243.47	370.87	48.68	29.02	205415.250	260.45	280.07	48.74	28.09	150784.867
3	246.65	376.02	49.56	29.85	205550.984	258.54	278.89	45.98	28.08	148989.589
4	246.65	376.02	49.56	29.85	205550.984	259.85	280.50	48.90	28.97	150799.759
5	246.62	376.02	49.58	29.83	205548.894	259.58	280.89	49.85	28.51	1507870.857
6	246.65	376.02	49.56	29.85	205550.984	259.58	280.89	49.85	28.51	1507870.857
7	246.57	376.08	49.57	29.75	205547.908	259.85	280.50	48.90	28.97	150799.759
8	246.62	376.02	49.58	29.83	205548.894	259.85	280.50	48.90	28.97	150799.759
9	246.78	376.95	50.83	29.88	205549.749	258.65	279.85	47.88	27.97	150745.598
10	247.75	377.99	51.50	30.00	205550.890	259.85	280.50	48.90	28.97	150799.759
11	**248.42**	**378.40**	**51.96**	**30.00**	**205582.593***	**261.49**	**281.02**	**49.50**	**29.30**	**150830.917***
12	245.56	378.02	50.98	29.98	205489.958	260.84	280.59	48.68	28.84	150798.915
13	**248.42**	**378.40**	**51.96**	**30.00**	**205582.593**	**261.49**	**281.02**	**49.50**	**29.30**	**150830.917**
14	245.14	377.58	50.51	29.75	205455.598	260.45	280.07	48.74	28.09	150784.867
15	**248.42**	**378.40**	**51.96**	**30.00**	**205582.593**	**261.49**	**281.02**	**49.50**	**29.30**	**150830.917**
16	243.47	370.87	48.68	29.02	205415.250	258.54	278.89	45.98	28.08	148989.589

* Bold numbers indicate the best solutions.

Table 6
The optimum results obtained by using SQP algorithm for two cases.

Parameter (mm)	Initial values		Optimum values			
	Case 1	Case 2	45°		90°	
			Case 1	Case 2	Case 1	Case 2
H	200	300	277.17	**255.03**	209.27	**313.93**
L	200	300	369.80	**350.95**	278.010	**390.44**
b_2	30	50	54.19	**51.32**	45.63	**51.28**
t	15	22.5	29.30	**29.89**	29.46	**26.31**
$F(\boldsymbol{X})$ (kN.mm)			180548.687	**183887.864***	146253.47	**148785.98**

* Bold numbers indicate the best solutions

Table 7
Comparison of the *ALLPD* to $PEEQ_{max}$ for the optimized USSD obtained by FE analysis and WLS-SVM.

Direction of loading	Method	FE analysis (kN.mm)	WLS-SVM (kN.mm)	Error (%)
90°	PSOPC	147752.035	150830.917	2.08
	SQP	144170.621	148785.98	3.20
45°	PSOPC	209399.863	205582.593	−1.82
	SQP	186385.430	183887.864	−1.34

where $\boldsymbol{I}$ and $\boldsymbol{O}$ are the input and output vectors of the WLS-SVM model, respectively. ns is the number of samples used. It should be noted that, in order to generate the data required for using the WLS-SVM approach, a limited number of analyses, approximately 5 percent of those required without using the approach, needs to be carried out using ABAQUS.

Fig. 6 illustrates the outline of the database generation procedure for training and testing the WLS-SVM by linking ABAQUS to MatLab [52]. Each of the elements of the input vectors ($\boldsymbol{X}$) was firstly transmitted to the ABAQUS pre-processing module for creating a USSD FE model. The entire FE analysis of the USSD subjected to cyclic loading was executed using a program in the framework of Python script. Then, the *ALLPD* to $PEEQ_{\max}$ ratio of the USSD was extracted from the ABAQUS output file using its post-processing module.

To validate the performance of the WLS-SVM model, some common performance metrics including the mean absolute percentage error (*MAPE*), the relative root-mean-squared error (*RRMSE*) and the absolute fraction of variance (R^2) are calculated in the testing process of the WLS-SVM model as:

$$MAPE = \frac{1}{n_t}\sum_{i=1}^{n_t} 100 \times \left|\frac{F_i - \bar{F}_i}{F_i}\right| \tag{17}$$

$$RRMSE = \sqrt{\frac{n_t \sum_{i=1}^{n_t} (F_i - \bar{F}_i)^2}{(n_t - 1)\sum_{i=1}^{n_t} F_i^2}} \tag{18}$$

Table 8
Comparison of the inelastic responses of the optimum-shaped USSD and UD40 [22].

Inelastic response	45°		90°	
	UD40	Optimized USSD	UD40	Optimized USSD
$PEEQ_{\max}$	0.2833	0.2224 (21.5%)	0.4183	0.3181 (23.9%)
ALLPD (kN.m)	41496.208	46567.764 (12%)	38068.004	47001.400 (23.5%)
$ALLPD/PEEQ_{\max}$ (kN.m)	146502.402	209399.863 (43%)*	78799.428	147752.035 (40.3%)

* The percentage of improvement.

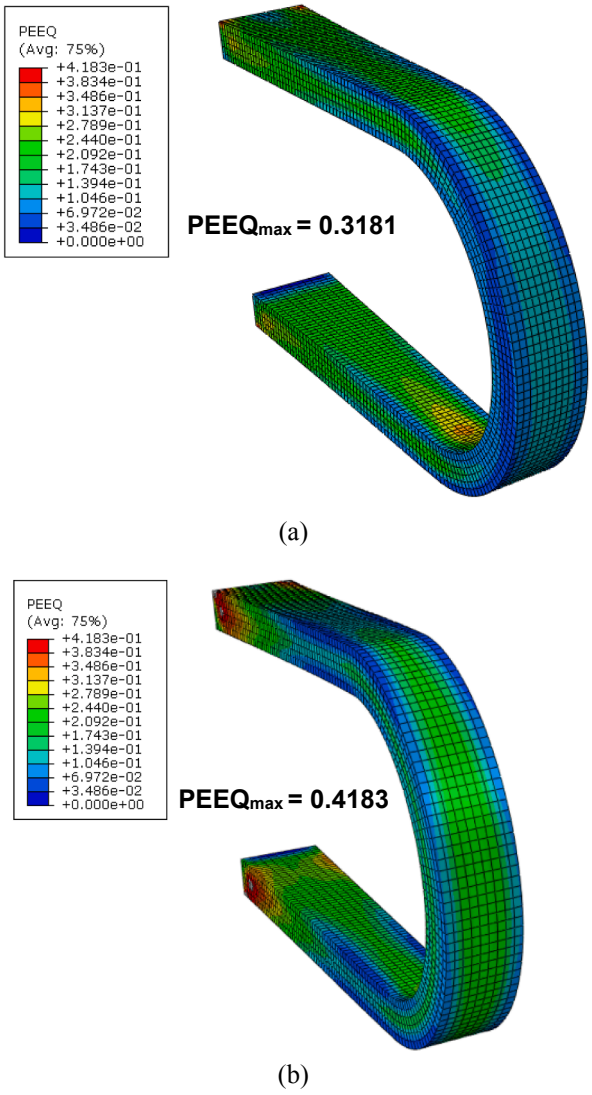

Fig. 10. The distribution of *PEEQ* for (a) the optimized USSD and (b) the UD40 [22] for 90° loading direction.

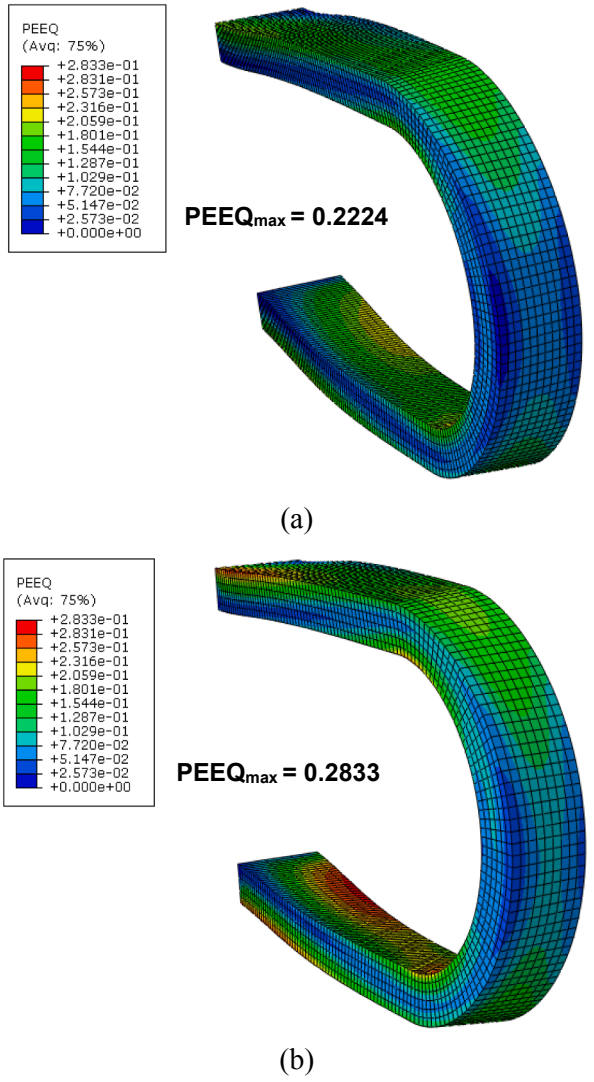

Fig. 11. The distribution of *PEEQ* for (a) the optimized USSD and (b) the UD40 [22] for 45° loading direction.

$$R^2 = 1 - \frac{\sum_{i=1}^{n_t} (F_i - \bar{F}_i)^2}{\sum_{i=1}^{n_t} \bar{F}_i^2} \tag{19}$$

where F and $\bar{F}$ are the actual and the predicted value, respectively; and n_t is the number of testing samples. It is noted that the smaller *RRMSE* and *MAPE* and the larger R^2 are indicative of better performance generality.

7. Numerical example

Herein, the shape optimization process of the USSD used in the work by Jiao et al. [22] was considered as the numerical example. The shape of the USSD was optimized under a loading protocol shown in Fig. 7 which is separately applied in two directions of 90° and 45°. The assumed lower and upper bounds of the design variables defined in Eq. (1) are listed in Table 2. It is noted that, b_1 is constant and equal to 70 mm. The generation of data and the optimization process is performed by an Intel Core i5 Duo 3.0 GHz CPU and the time of all computations is evaluated in clock time.

7.1. Training and testing the WLS-SVM model

To provide a database for training and testing the WLS-SVM model, first, a set of combinations of the design variables of the USSD including 200 samples was generated using the Latin Hypercube sampling technique [53] for each of the 90° and 45° loading directions. These selected USSDs were analysed by the ABAQUS software and their *ALLPD* and $PEEQ_{max}$ responses were obtained. The total time spent on the data generation for the 90° and 45° loading directions was about 18,000 and 17575 min (i.e. about 13 and 12 days), respectively. Then, the generated samples for both loading directions were randomly divided into the training and testing sets including 140 and 60 samples, respectively. In the training phase of the WLS-SVM model, the 10-fold cross-validation and the grid searching method [38] were employed to find the optimum values of γ and σ. Therefore, for the 90° and 45° loading directions, the results of performance metrics of the WLS-SVM model in the testing mode are given in Table 3. It can be observed from Table 3 that the WLS-SVM model provides low *MAPE* and *RRMSE* and high R^2 indicating that the predicted responses are in an excellent agreement with actual ones. The predicted values of *ALLPD* to $PEEQ_{max}$ by WLS-SVM are also compared with their corresponding actual ones in Fig. 8, indicating the accuracy of the predictive model. This can efficiently reduce the overall computational time of the optimization

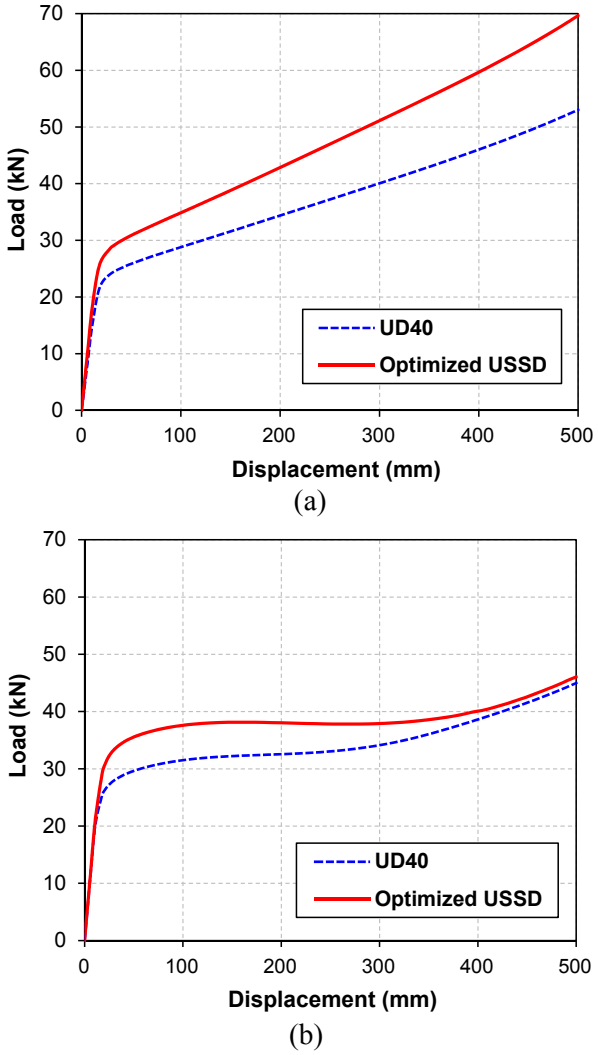

Fig. 12. Comparison of the pushover curves of the optimized USSD and UD40 [22] for (a) 90° and (b) 45° loading direction.

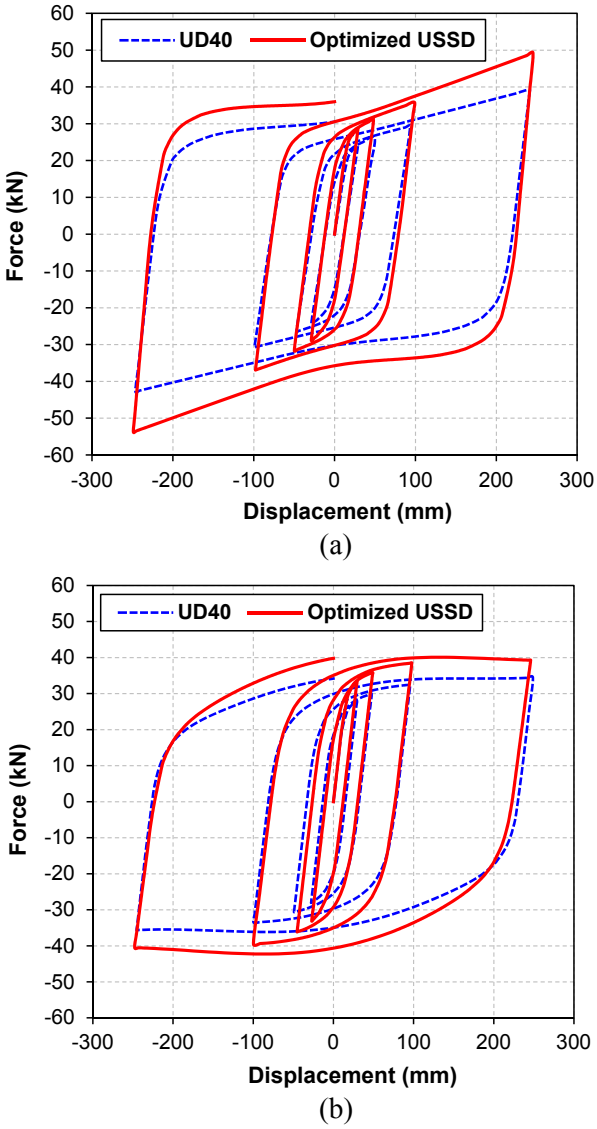

Fig. 13. Comparison of the hysteresis curve between the optimized USSD and UD40 [22] for (a) 90° and (b) 45° loading direction.

procedure. The elapsed time of training the WLS-SVM model for 90° and 45° loading directions was 1.8 and 1.65 min, respectively.

It should be noted that the elapsed time to analysis of one FE model of the USSD subjected to cyclic loading is almost 90 min. Given this information, assuming 30 populations and 200 iterations for executing the shape optimization problem of the USSD using PSOPC algorithm, the required time is approximated as 540,000 min which is very expensive. This main challenging issue confirms the efficiency of WLS-SVM model in such computationally expensive optimization problems. Fig. 9 shows the convergence of the objective function over 200 iterations for both loading directions.

7.2. The results of optimization

To solve the optimization process, the population size (N) and the maximum number of iterations (t_{max}) of the PSOPC algorithm were set to 30 and 200, respectively. In order to investigate the effect of input user-defined parameters in the PSOPC algorithm on the shape optimum design of the USSD, different values of the parameters listed in Table 4 were given. These parameters were selected based on the general recommendations given in the literature [39–41]. The cognitive, social scaling and passive congregation factors were selected from the sets $c_1 = \{0.5, 1.0, 1.5, 2.0\}$, $c_2 = \{1.5, 2.0\}$ and $c_3 = \{0.5, 0.6\}$, respectively. The minimum and maximum inertia weights were assumed from the sets $\omega_{min} = \{1.5, 2.0\}$ and $\omega_{max} = \{0.1, 0.4\}$, respectively. Based on the stochastic nature of the PSOPC algorithm, 10 independent runs were first implemented for each case for both 90° and 45° loading directions. Then, the final obtained design vector corresponding to the maximum value of the objective function was selected as the best optimum dimensions of the optimized USSD. The optimum dimensions of each case obtained for the 90° and 45° directions of cyclic loading are presented in Table 5. As can be seen from Table 5, the variation of the user-defined parameters can affect the performance of the PSOPC algorithm. It reveals from Table 5 that the optimum shapes of the USSD for the 90° and 45° loading directions are different. Except for the height H, almost the remained dimensions of the optimized USSD for 45° loading direction are greater than those for 90° loading direction.

In order to demonstrate the disability of local search algorithms in finding the global solution of the shape optimization problem of the damper, the optimum shape design of the USSD was also found by using the SQP algorithm [54]. For this purpose, the SQP algorithm was run from two different starting points on the domain (denoted as Case 1 and Case 2) for both 90° and 45° loading directions. The results of the SQP algorithm were obtained and shown in Table 6. It is evident from Tables 5 and 6 that the PSOPC algorithm provides better results than SQP

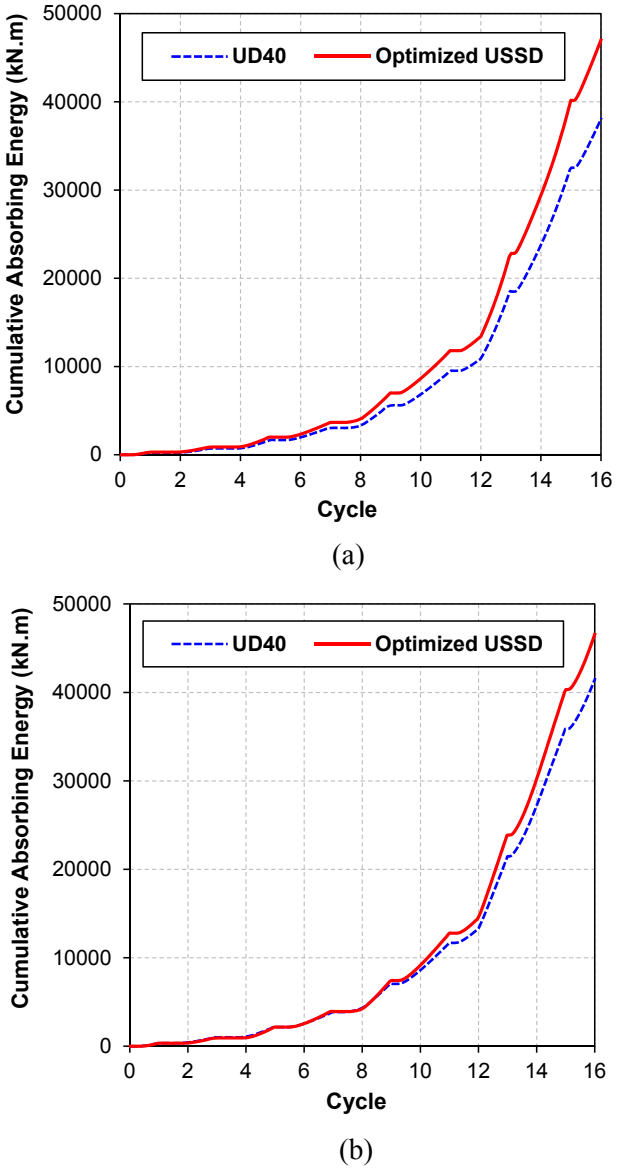

Fig. 14. Comparison of the cumulative absorbing energy between the optimized USSD and UD40 [22] for (a) 90° and (b) 45° loading direction.

algorithm in the optimum shape design of the USSD. Therefore, the PSOPC algorithm could be used as a promising tool for the (near) global optimization shape of the USSD as the defined problem could be considered as a multimodal optimization problem.

In order to assess the performance of the WLS-SVM model in the optimization procedure and to evaluate the behaviour of the optimum USSDs obtained by the PSOPC and SQP algorithms, they were analysed under both 90° and 45° loading directions using ABAQUS. The actual value of the objective function ($ALLPD/PEEQ_{max}$) for both loading directions was determined using ABAQUS to be compared with the predicted ones. The results of the comparison are shown in Table 7. As can be seen from Table 7, the percentage of errors for the PSOPC algorithm is 2.08% and 1.82% respectively for the 90° and 45° loading directions, while for the SQP algorithm the value is 3.2% and 1.34% for the 90° and 45° loading directions, respectively. These low errors indicate that the WLS-SVM model could reliably be used in the optimization procedure instead of the FE analysis by means of ABAQUS as it could accurately predict the inelastic responses of the USSD.

7.3. Performance evaluation of the optimized USSDs

In order to demonstrate the effectiveness of the presented shape optimization procedure in improving the performance of the USSD, the performance of the optimized USSD and UD40 [22] subjected to the cyclic loading (Fig. 7) were evaluated to be compared. For this purpose, the optimized USSD and UD40 corresponding to 90° and 45° directions of cyclic loading were analyzed by ABAQUS and their inealstic responses including *ALLPD* and $PEEQ_{max}$ were obtained. The inealstic responses are listed in Table 8. As can be seen from Table 8, the *ALLPD* of the optimized USSD for 90° and 45° loading directions is increased to 47001.4 and 46567.764 kN.m which are almost 23.5% and 12% more than those for UD40, respectively. The $PEEQ_{max}$ of the optimized USSD for the 90° and 45° loading directions is also decreased to 0.3181 and 0.2224 which are 23.9% and 21.5% less than those for UD40, respectively. Finally, the ratio of *ALLPD* to $PEEQ_{max}$ is almost 40.3% and 43% more than those for UD40 respectively for 90° and 45° loading directions indicating the excellent performance of the proposed optimization framework.

The distribution of *PEEQ* for the optimized USSD and UD40 under cyclic loading is also depicted in Figs. 10 and 11 for the 90° and 45° loading directions, respectively. As shown in these figures, for both loading directions, the distribution of *PEEQ* is more uniform than those for UD40. This is resulted in decreasing in the $PEEQ_{max}$ and residual deformation of the optimized USSD compared with those for UD40. This means that the concentration of plastic strain is avoided by the defined optimization problem, indicating the improvement of deformation capability of the optimized USSD compared with UD40.

The pushover curves of the optimized USSD and UD40 are determined for both 90° and 45° loading directions at the same displacement amplitude. As shown in Fig. 12, the defined optimization problem results in a strengthened USSD rather than UD40. This also would result in more energy ductility ratio for the optimized USSD compared with those for UD40.

Next, the energy dissipation capability of the optimized USSD and UD40 are compared. The hysteresis curve of the optimized USSD for both 90° and 45° loading directions are shown in Fig. 13. As shown in this figure, for both loading directions, the hysteretic curves of the optimized USSD are more stable than those for UD40. As the displacement amplitude of the applied cyclic loading is the same, this advantage is rooted in the higher strength of the optimum-shaped USSD compared with UD40. Moreover, as shown in Fig. 14, the cumulative absorbing energy of the optimized USSD and UD40 are assessed based on their absorbed energy through the loading cycles exerted in the both 90° and 45° loading directions. Based on this figure, after almost 8 and 11 cycles respectively for 90° and 45° loading directions where the significant plastic deformations are occurred, the cumulative absorbing energy of the optimized USSD is more than those for UD40. The maximum cumulative absorbing energy of the optimized USSD is almost 17% and 20% more than those for UD40, for 90° and 45° loading directions, respectively.

Finally, the superior performance of the optimized USSD compared with UD40 validates the efficiency of the shape optimization framework presented in this paper.

8. Conclusion

In this paper, the shape design of a USSD was proposed in the framework of an optimization problem in order to improve its energy dissipation and deformation capability subjected to 90° and 45° directions of cyclic loading. The ratio of *energy dissipation through plastic deformation* to the *maximum cumulative equivalent plastic strain* ($ALLPD/PEEQ_{max}$), as a single objective function of the shape optimization problem, was maximized through the optimization problem defined. The influential dimensions of the USSD including the straight part, thickness, width and height of the USSD were considered as the design

variables. A soft computing-based approach based on hybridizing the PSOPC algorithm and the WLS-SVM approach was presented to solve the optimization problem. In fact, the PSOPC algorithm was adapted to progress the optimization procedure defined and the WLS-SVM approach was used to effectively predict the results of the inelastic analyses needed during the optimization procedure. Several FE models were created in the ABAQUS software to determine the inelastic behavior of the USSD subjected to cyclic loading and to generate the sample dataset as inputs of the WLS-SVM model. The main conclusions of this study are as follows:

- The optimum design of the USSD subjected to cyclic loading was efficiently found by the presented soft computing-based hybrid approach.
- The WLS-SVM approach accurately predicts the inelastic responses of the USSD during the optimization process, resulting in reducing the elapsed time of the optimization procedure.
- The proposed optimum-shaped USSDs show a significant improvement in the energy dissipation and deformation capability in comparison with the conventional U-shaped steel damper proposed in the literature.

Moreover, as the results of the shape optimization technique, the optimum-shaped USSD shows more strength capacity and energy ductility ratio compared with the conventional U-shaped steel damper proposed in the literature.

Appendix A. Supplementary material

Supplementary data to this article can be found online at https://doi.org/10.1016/j.engstruct.2019.02.005.

References

[1] Wong KK. Seismic energy dissipation of inelastic structures with tuned mass dampers. J Eng Mech 2008;134:163–72.
[2] Shayesteh Bilondi MR, Yazdani H, Khatibinia M. Seismic energy dissipation-based optimum design of tuned mass dampers. Struct Multidisc Optim 2018. https://doi.org/10.1007/s00158-018-2033-0.
[3] Mahmoudi M, Abdi MG. Evaluating response modification factors of TADAS frames. J Constr Steel Res 2012;71:162–70.
[4] Saeedi F, Shabakhty N, Mousavi SR. Seismic assessment of steel frames with triangular-plate added damping and stiffness devices. J Constr Steel Res 2016;125:15–25.
[5] Sorace S, Terenzi G, Mori C. Passive energy dissipation-based retrofit strategies for R/C frame water storage tanks. Eng Struct 2016;106:385–98.
[6] De Matteis G, Brando G, Panico S, Mazzolani FM. Bracing type pure aluminium stiffened shear panels: An experimental study. Adv Steel Constr 2009;5:106–19.
[7] Kang THK, Martin RD, Park HG, Wilkerson R, Youssef N. Tall building with steel plate shear walls subject to load reversal. Struct Des Tall Spec Build 2013;22:500–20.
[8] Jain S, Rai DC, Sahoo DR. Postyield cyclic buckling criteria for aluminum shear panels. J Appl Mech Trans ASME 2008;75:210151–8.
[9] Hamed AA, Mofid M. On the equivalent simple models of braced steel shear panels. Proc Inst Civil Eng Struct Build 2015;168:570–7.
[10] Hamed AA, Mofid M. On the experimental and numerical study of braced steel shear panels. Struct Des Tall Spec Build 2015;24:853–72.
[11] Zhang C, Zhu J, Wu M, Yu J, Zhao J. The lightweight design of a seismic low-yield-strength steel shear panel damper. Materials 2016;9:424.
[12] Vian D, Bruneau M, Purba R. Special perforated steel plate shear walls with reduced beam section anchor beams. II: Analysis and design recommendations. J Struct Eng 2009;135:221–8.
[13] Valizadeh H, Sheidaii M, Showkati H. Experimental investigation on cyclic behavior of perforated steel plate shear walls. J Constr Steel Res 2012;70:308–16.
[14] Chan RWK, Albermani F, Kitipornchai S. Experimental study of perforated yielding shear panel device for passive energy dissipation. J Constr Steel Res 2013;91:14–25.
[15] Egorova N, Eatherton MR, Maurya A. Experimental study of ring-shaped steel plate shear walls. J Constr Steel Res 2014;103:179–89.
[16] De Matteis G, Sarracco G, Brando G. Experimental tests and optimization rules for steel perforated shear panels. J Constr Steel Res 2016;123:41–52.
[17] Brando G, D'Agostino F, De Matteis G. Experimental tests of a new hysteretic damper made of buckling inhibited shear panels. Mater Struct 2013;46:2121–33.
[18] Deng K, Pan P, Li W, Xue Y. Development of a buckling restrained shear panel damper. J Constr Steel Res 2015;106:311–21.
[19] Qu B, Liu X, Hou H, Qiu C, Hu D. Testing of buckling-restrained braces with replaceable steel angle fuses. J Struct Eng 2018;144.
[20] Lin PC, Tsai KC, Chang CA, Hsiao YY, Wu AC. Seismic design and testing of buckling-restrained braces with a thin profile. Earthq Eng Struct Dyn 2016;45:339–58.
[21] Shoichi K, Yuta O, Satoshi Y, Akira W. Experimental evaluation of cyclic deformation capacity of u-shaped steel dampers for base isolated structures. J Struct Constr Eng 2008;624:333–40.
[22] Jiao Y, Kishiki Sh, Yamada S, Ene D, Konishi Y, Hoashi Y, et al. Low cyclic fatigue and hysteretic behavior of U-shaped steel dampers for seismically isolated buildings under dynamic cyclic loadings. Earthquake Engng Struct Dyn 2015;44(10):1523–38.
[23] Ene D, Kishiki Sh, Yamada S, Jiao Y, Konishi Y, Terashima M, et al. Experimental study on the bidirectional inelastic deformation capacity of U-shaped steel dampers for seismic isolated buildings. Earthquake Engng Struct Dyn 2016;45:173–92.
[24] Kelly JM, Skinner RI, Heine AJ. Mechanisms of energy absorption in special devices for use in earthquake-resistant structures. Bull N Z Natl Soc Earthq Eng 1972;5(3):63–88.
[25] Aguirre M, Sanchez AR. Structural seismic damper. J Struct Eng ASCE 1992;118(5):1158–71.
[26] Dolce M, Filardi B, Marnetto R, Nigro D. Experimental tests and applications of a new biaxial elasto-plastic device for the passive control of structures. Fourth world congress on joint sealants and bearing systems for concrete structures, ACI SP–164, Sacramento, California; 1996.
[27] Suzuki K, Watanabe A, Saeki E. Development of U-shaped steel damper for seismic isolation system. Nippon Steel Technical Report, No. 92; 2005.
[28] Deng K, Pan P, Wang C. Development of crawler steel damper for bridges. J Constr Steel Res 2013;85:140–50.
[29] Bagheri S, Barghian M, Saieri F, Farzinfar A. U-shaped metallic-yielding damper in building structures: Seismic behavior and comparison with a friction damper. Structures 2015;3:163–71.
[30] Sun SH, Yu TT, Nguyen TT, Atroshchenko E, Bui TQ. Structural shape optimization by IGABEM and particle swarm optimization algorithm. Eng Anal Bound Elem 2018;88:26–40.
[31] Braibant V, Fleury C. Shape optimum design using B–splines. Comput Methods Appl Mech Eng 1984;44:247–67.
[32] Ding Y. Shape optimization of structures: a literature survey. Comput Struct 1986;24(6):985–1004.
[33] Olhoff N, Rozvany G. Structural and multidisciplinary optimization. Oxford: Pergamon Press; 1995.
[34] Munk DJ, Vio1 GA, Steven GP. Topology and shape optimization methods using evolutionary algorithms: a review. Struct Multidisc Optim 2015;52:613–31.
[35] Deng K, Pan P, Su Y, Xue Y. Shape optimization of U-shaped damper for improving its bi-directional performance under cyclic loading. Eng Struct 2015;93:27–35.
[36] Rao SS. Engineering optimization theory and practice. 4th ed. USA: John Wiley & Sons; 2009.
[37] He S, Wu QH, Wen JY, Saunders JR, Paton RC. A particle swarm optimizer with passive congregation. Biosystems 2004;78:135–47.
[38] Suykens JAK, Brabanter JD, Lukas L, Vandewalle J. Weighted least squares support vector machines: robustness and sparse approximation. Neurocomputing 2002;48:85–105.
[39] Gharehbaghi S, Khatibinia M. Optimum seismic design of reinforced concrete structures under time-history earthquake loads using an intelligent hybrid algorithm. Earth Eng Eng Vib 2015;14:97–109.
[40] Gharehbaghi S, Moustafa A, Salajegheh E. Optimum seismic design of reinforced concrete frame structures. Comput Con 2016;17(6):761–86.
[41] Gharehbaghi S. Damage controlled optimum seismic design of reinforced concrete framed structures. Struct Eng Mech 2018;65(1):53–68.
[42] Kennedy J, Eberhart R. Particle swarm optimization. In: Proceedings of IEEE international conference on neural networks. Perth, Australia; 1995. p. 1942–48.
[43] Shi Y, Eberhart R. A modified particle swarm optimizer. In: 1998 IEEE international conference on evolutionary computation proceedings. IEEE World Congress on Computational Intelligence (Cat. No.98TH8360); 1998. p. 69–73.
[44] ABAQUS, Analysis user's manual-version 6.4, 19.2.2. Hbbit, Karlsson & Sorensen, Inc; 2003.
[45] Jirásek M, Bazant Z. Inelastic analysis of structures. Chichester, West Sussex, England: Wiley; 2002.
[46] Lemaître J, Chaboche JL. Mechanics of solid materials. Cambridge: Cambridge University Press; 1990.
[47] Khatibinia M, Fadaee MJ, Salajegheh J, Salajegheh E. Seismic reliability assessment of RC structures including soil-structure interaction using wavelet weighted least squares support vector machine. Reliab Eng Syst Safe 2013;110:22–33.
[48] Khatibinia M, Salajegheh E, Salajegheh J, Fadaee MJ. Reliability-based design optimization of RC structures including soil–structure interaction using a discrete gravitational search algorithm and a proposed metamodel. Eng Optimiz 2013;45(10):1147–65.
[49] Khatibinia M, Khosravi Sh. A hybrid approach based on an improved gravitational search algorithm and orthogonal crossover for optimum shape design of concrete gravity dams. Appl Soft Comput 2014;16:223–33.
[50] Khatibinia M, Gharehbaghi S, Moustafa A. Seismic reliability-based design optimization of reinforced concrete structures including soil-structure interaction effects. Earthquake Eng-From Eng Seismol Optimum Seismic Des Eng Struct 2015:267–304.
[51] Yazdani H, Khatibinia M, Gharehbaghi S, Hatami K. Probabilistic performance-based optimum seismic design of RC structures considering soil-structure interaction effects. ASCE-ASME J Risk Uncertain Eng Syst Part Civ Eng 2017;3:G4016004.
[52] Mathworks Inc. Matlab R2011a; 2011.
[53] Mckay MD, Beckman RJ, Conover WJ. A comparison of three methods for selecting values on input variables in the analysis of output from a computer code. Technometrics 1971;21:439–45.
[54] Boggs PT, Tolle JW. Sequential quadratic programming. Acta Numeric 1995;4:1–52.